Target-oriented wavefield tomography using demigrated Born data

Yaxun Tang and Biondo Biondi, Stanford University*

SUMMARY

We present a method to reduce the computational cost of image-domain wavefield tomography. Instead of using the originally recorded data for velocity estimation, the proposed method simulates a new data set obtained using Born modeling or demigration based on the initial image and gathers. The modeling can be performed in a target-oriented fashion, and it can use arbitrary types of source functions and acquisition geometries. Hence the size of the new data set can be substantially smaller than the original one. We demonstrate with numerical examples that the new data set correctly preserves velocity information useful for velocity estimation, and that it generates wavefield-tomography gradient similar to that obtained using the original data set. We apply the proposed method to a modified version of the Sigsbee2A model, where two square anomalies below the salt have been successfully recovered in a target-oriented fashion at much lower computational cost.

INTRODUCTION

Velocity estimation is always a challenging task in exploration seismology. In the past decade, ray-based tomography has been widely used in practice to derive velocity models. Although ray-based methods are efficient, the infinite-frequency approximation and the caustics inherent in ray theory prevent them from accurately modeling complicated wave phenomena (Hoffmann, 2001). As seismic exploration is moving towards structurally complex areas, ray-based methods become less reliable. On the other hand, wave-equation-based tomography (Tarantola, 1984; Mora, 1989; Woodward, 1992; Pratt, 1999; Sava, 2004; Shen, 2004) uses wavefields as carriers of information. It more accurately describes the bandlimited wave phenomena, and therefore more suitable for complex geologies.

Wavefield tomography can be implemented in either data domain or image domain. In this paper, however, we mainly focus on the image-domain wavefield tomography, which is also widely known as wave-equation migration velocity analysis (Sava, 2004; Shen, 2004). It derives an optimum velocity model by driving an image-domain defined objective function to its minimum. Despite its advantages in modeling bandlimited wavefields, practical application of image-domain wavefield tomography is still rare and small in scale due to its huge computational cost (Biondi and Sava, 1999; Shen et al., 2005; Albertin et al., 2006). The high cost arises because of the use of more expensive wavefield modeling engines. The other reason is that it lacks flexibility and the recorded full data set is usually used for velocity estimation.

Several methods have been proposed to make wavefield tomography more cost effective. The main idea is to reduce the size of the data used for velocity estimation. One method is to assemble the originally recorded point-source gathers into a smaller number of areal-source gathers. Among the others, plane-wave-source gather (Whitmore, 1995; Zhang et al., 2005; Shen and Symes, 2008; Tang et al., 2008) is the most popular one because the plane-wave-phase-encoding function is effective in attenuating the crosstalk artifacts (Liu et al., 2006; Tang, 2008). The other method is to model a new data set in a target-oriented fashion using the concept of prestack-exploding-reflector modeling with a bottom-up strategy (Biondi, 2006, 2007; Guerra et al., 2009). However, the modeling generates crosstalk when multiple image events are modeled simultaneously. Stochastic encoding method, such as random-phase encoding, seems to be the only encoding method available to attenuate the crosstalk produced when imaging the image-domain encoded gathers (Guerra and Biondi, 2008a,b).

In this paper, we present a new strategy to reduce the size of the data set used for image-domain wavefield tomography. The proposed strategy combines advantages of both prestack-exploding-reflector modeling and data-domain encoding: Not only can it model a new data set in a target-oriented fashion, but also use plane-wave sources to effectively attenuate the crosstalk. We start with an initial image and gathers (obtained using a starting velocity model), instead of using prestack-exploding-reflector modeling, we use Born modeling or demigration (Stolt and Benson, 1986) to simulate the new data set. The modeling procedure is based on single-scattering approximation to the full wave equation, and the resulting Born modeled data is obtained by convolving the source wavefield, computed using any types of source functions (e.g. plane-wave sources), with the initial image and gathers and then propagating the convolved wavefields to receiver locations, which can be located anywhere in the model. The target-oriented data set is obtained by only modeling image points within a target zone or several key reflectors that carry important velocity information. This target-oriented velocity analysis strategy is useful, because it allows us to use the most powerful velocity estimation tool to focus on improving velocities in the most challenging areas, e.g., subsalt regions, provided that velocities at other locations are sufficiently accurate, e.g., regions above the salt, where the velocities are usually very accruately determined even by ray-based tomography thanks to the relatively simple geologies. In the next section, we briefly review the theory of Born modeling. In the subsequent sections, we apply the proposed target-oriented velocity-estimation method to invert the local velocity anomalies in a modified Sigsbee2A model.

TARGET-ORIENTED BORN WAVEFIELD MODELING

Seismic images can be obtained by applying shot-profile migration to the recorded data as follows:

$$m(\mathbf{x},\mathbf{h}) \quad = \quad \sum_{\omega}\sum_{\mathbf{x}_s} G_0^*(\mathbf{x}-\mathbf{h},\mathbf{x}_S,\omega)\sum_{\mathbf{x}_r} W(\mathbf{x}_r,\mathbf{x}_s)$$

$$\times G_0^*(\mathbf{x}+\mathbf{h},\mathbf{x}_r,\omega)d(\mathbf{x}_r,\mathbf{x}_s,\omega) \quad (1)$$

where * denotes adjoint and $m(\mathbf{x},\mathbf{h})$ is the migrated image as a function of both image point $\mathbf{x}=(x,y,z)$ and subsurface half offset $\mathbf{h}=(h_x,h_y,h_z)$. The frequency-domian data $d(\mathbf{x}_r,\mathbf{x}_s,\omega)$ is recorded at receiver position $\mathbf{x}_r=(x_r,y_r,0)$ due to a source located at $\mathbf{x}_s=(x_s,y_s,0)$; $W(\mathbf{x}_r,\mathbf{x}_s)$ is the acquisition mask operator, which contains unity values where we record data and zero values where we do not; $G_0(\mathbf{x},\mathbf{x}_s,\omega)$ and $G_0(\mathbf{x},\mathbf{x}_r,\omega)$ are the Green's functions connecting the source and receiver, respectively, to image point $\mathbf{x}$. The Green's functions are obtained using a starting velocity model $\mathbf{v}_0$. Throughout this paper, we perform numerical examples using Greens functions computed by means of one-way wavefield extrapolation (Claerbout, 1985; Stoffa et al., 1990; Ristow and Rühl, 1994; Biondi, 2002). Although not tested here, Greens functions obtained using other methods, such as by solving the two-way wave equation, also can be used under this framework. Since the one-way wavefield extrapolator has limited accuracy for large-angle propagation, we only compute horizontal half subsurface offset, i.e., $\mathbf{h}=(h_x,h_y,0)$.

We use Born modeling (Stolt and Benson, 1986) to simulate a new data set based on the initial image obtained using equation 1. The modeling can be performed using arbitrary source functions and arbitrary acquisition geometries. The modeled data set using encoded areal sources reads (Tang, 2008)

$$\begin{aligned}\widetilde{d}(\mathbf{p}_s,\widetilde{\mathbf{x}}_r,\omega) &= \sum_{\widetilde{\mathbf{x}}}\sum_{\mathbf{h}} G_0(\widetilde{\mathbf{x}}-\mathbf{h},\mathbf{p}_s,\omega)\\ &\quad\times G_0(\widetilde{\mathbf{x}}+\mathbf{h},\widetilde{\mathbf{x}}_r,\omega)m(\widetilde{\mathbf{x}},\mathbf{h}),\end{aligned} \quad (2)$$

where $\widetilde{\mathbf{x}}=(\widetilde{x},\widetilde{y},\widetilde{z})$ is an image point belonging to the selected target zone; $\widetilde{\mathbf{x}}_r=(\widetilde{x}_r,\widetilde{y}_r,\widetilde{z}_r)$ is the receiver location used for modeling, it can differ substantially from the original receiver location $\mathbf{x}_r$, which can be only on the surface, i.e., $\mathbf{x}_r=(x_r,y_r,0)$; $G_0(\widetilde{\mathbf{x}},\mathbf{p}_s,\omega)$ is the Green's function obtained using the encoded areal source, it can be written as a weighted sum of point-source Green's functions as follows:

$$G_0(\widetilde{\mathbf{x}},\mathbf{p}_s,\omega)=\sum_{\widetilde{\mathbf{x}}_s} G_0(\widetilde{\mathbf{x}},\widetilde{\mathbf{x}}_s,\omega)\alpha(\widetilde{\mathbf{x}}_s,\mathbf{p}_s,\omega), \quad (3)$$

where $\alpha(\widetilde{\mathbf{x}}_s,\mathbf{p}_s,\omega)$ and $\mathbf{p}_s$ are the encoding function and encoding index, respectively, to be specified later. Similar to the new receiver location $\widetilde{\mathbf{x}}_r$, the new source location $\widetilde{\mathbf{x}}_s=(\widetilde{x}_s,\widetilde{y}_s,\widetilde{z}_s)$ can also be substantially different from the original source location $\mathbf{x}_s$. Note in particular that the Green's function used for modeling ($G_0(\widetilde{\mathbf{x}},\mathbf{p}_s,\omega)$) is computed using the same velocity model ($\mathbf{v}_0$) as that used for migrating the original data. Therefore, the modeling process undoes the effect of the starting velocity model $\mathbf{v}_0$ (at least in kinematics), resulting in a starting-velocity-independent data set.

The synthesized areal data can be imaged by using conventional migration of areal-source data as follows:

$$\begin{aligned}\widehat{m}(\widetilde{\mathbf{x}},\mathbf{h}) &= \sum_{\omega}\sum_{\mathbf{p}_s} G^*(\widetilde{\mathbf{x}}-\mathbf{h},\mathbf{p}_s,\omega)\\ &\quad\times\sum_{\widetilde{\mathbf{x}}_r} G^*(\widetilde{\mathbf{x}}+\mathbf{h},\widetilde{\mathbf{x}}_r,\omega)\widetilde{d}(\mathbf{p}_s,\widetilde{\mathbf{x}}_r,\omega),\end{aligned} \quad (4)$$

where Green's functions G's are obtained using velocity model $\mathbf{v}$, which can be the same or different from the starting velocity model $\mathbf{v}_0$, to be discussed later. Imaging the areal-source data using equation 4, however, generates crosstalk artifacts (Romero et al., 2000; Liu et al., 2006; Tang, 2008). To attenuate the crosstalk, the encoding function α is chosen such that

$$\sum_{\mathbf{p}_s}\alpha(\widetilde{\mathbf{x}}_s,\mathbf{p}_s,\omega)\alpha(\widetilde{\mathbf{x}}'_s,\mathbf{p}_s,\omega)\approx\delta(\widetilde{\mathbf{x}}_s-\widetilde{\mathbf{x}}'_s), \quad (5)$$

where $\delta(\cdot)$ is the Dirac delta function. For plane-wave-phase encoding, $\alpha(\widetilde{\mathbf{x}}_s,\mathbf{p}_s,\omega)=A(\omega)e^{i\omega\mathbf{p}_s\cdot\widetilde{\mathbf{x}}_s}$, with $A^2(\omega)=|\omega|$ in two dimensions and $A^2(\omega)=|\omega|^2$ in three dimensions, and $\mathbf{p}_s=(p_{s_x},p_{s_y},0)$ is the ray parameter for the source plane waves at depth level $\widetilde{z}_s$.

Substituting equations 3 and 2 into equation 4 yields

$$\widehat{m}(\widetilde{\mathbf{x}},\mathbf{h})=\sum_{\widetilde{\mathbf{x}}'}\sum_{\mathbf{h}'}\Delta G(\widetilde{\mathbf{x}},\mathbf{h},\widetilde{\mathbf{x}}',\mathbf{h}')m(\widetilde{\mathbf{x}}',\mathbf{h}'), \quad (6)$$

where

$$\begin{aligned}\Delta G(\widetilde{\mathbf{x}},\mathbf{h},\widetilde{\mathbf{x}}',\mathbf{h}') &= \sum_{\omega,\widetilde{\mathbf{x}}_s,\widetilde{\mathbf{x}}_r} G^*(\widetilde{\mathbf{x}}-\mathbf{h},\widetilde{\mathbf{x}}_s,\omega)G_0(\widetilde{\mathbf{x}}'-\mathbf{h}',\widetilde{\mathbf{x}}_s,\omega)\\ &\quad\times\ G^*(\widetilde{\mathbf{x}}+\mathbf{h},\widetilde{\mathbf{x}}_r,\omega)G_0(\widetilde{\mathbf{x}}'+\mathbf{h}',\widetilde{\mathbf{x}}_r,\omega).\end{aligned} \quad (7)$$

When the same velocity model has been used for Born modeling and migration ($\mathbf{v}_0=\mathbf{v}$), $\Delta G(\widetilde{\mathbf{x}},\mathbf{h},\widetilde{\mathbf{x}}',\mathbf{h}')$ becomes the local Hessian operator or resolution function (Lecomte, 2008; Valenciano, 2008; Tang, 2009), which is of zero phase and centered at $\widetilde{\mathbf{x}}'=\widetilde{\mathbf{x}}$ and $\mathbf{h}'=\mathbf{h}$. Therefore, $\widehat{m}(\widetilde{\mathbf{x}},\mathbf{h})$ is a filtered version of the original image, $m(\widetilde{\mathbf{x}},\mathbf{h})$. They have completely the same kinematics. When the migration velocity is different from the modeling velocity ($\mathbf{v}_0\neq\mathbf{v}$), the two images may substantially differ. Because we want to use migration results to estimate velocity, it is important to demonstrate that the velocity information contained in the prestack image obtained from the data modeled using the proposed procedure is consistent with the velocity information extracted from the prestack image obtained from migrating the originally recorded data set.

Figure 1(a) shows a modified Sigsbee2A velocity model, which contains two square anomalies below the salt: one 10% lower and the other 10% higher than the sediment velocity. We model 268 shots using two-way wave-equation with a time-domain finite-difference scheme. The data is recorded with a marine acquisition geometry, the maximum offset for each shot is about 26000 ft. We refer this two-way data set as "original data" hereafter. The migrated prestack image and gathers using the original data and a starting velocity model (Figure 1(b)) are shown in Figure 2. The amplitude of the background image has been normalized by the diagonal of the phase-encoded Hessian (not shown here) to partially compensate uneven illumination (Tang, 2009). Note the unfocused subsurface-offset-domain common-image gathers (SODCIGs) due to velocity errors. Then we use the target image (Figure 2) and the Born modeling described above to generate 41 plane-wave-source gathers from depth level $\widetilde{z}_s=15500$ ft, the take-off angle is from -45° to 45°. The same starting velocity model that was used for migration (Figure 1(b)) has been used for modeling

and the new data set is collected just above the target region, i.e., $\widetilde{z}_r = \widetilde{z}_s = 15500$ ft. We refer the Born data as "new data" hereafter. The plane-wave migration result of the new data set using the starting velocity model is shown in Figure 3. Note the same kinematics shown in Figures 2 and 3. This suggests that the velocity information has been successfully preserved using the new data set, which is substantially smaller compared to the original one. Also note that Figure 3 is more blurry than Figure 2 due to the filtering effect of the resolution function ΔG (equation 7).

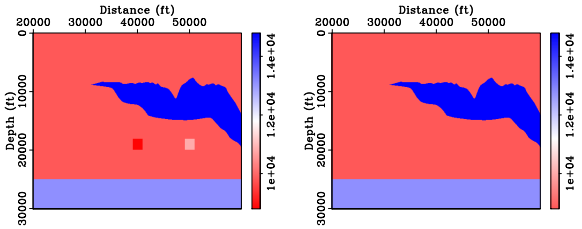

Figure 1: (a) The modified Sigsbee2A velocity model and (b) the starting velocity model.

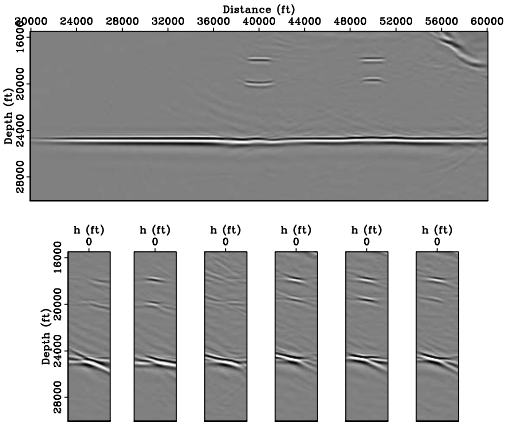

Figure 2: Initial image obtained using the original two-way finite-difference modeled data. The image has been normalized using the diagonal of the phase-encoded Hessian. Top: zero-subsurface offset image (stacked image), bottom: SODCIGs at surface location 38575,40000,41425,49300,50000 and 50700 ft, respectively.

TOMOGRAPHY USING DEMIGRATED DATA

The objective function of image-domain wavefield tomography can be defined as the ℓ_2 norm of either an image-domain residual field (Sava, 2004; Shen, 2004) or the negative image-stack power (or image coherence) (Toldi, 1985; Soubaras and Gratacos, 2007) or both (Shen and Symes, 2008). A widely used residual operator is the subsurface-offset-domain differential semblance optimization (DSO) operator, where the velocity model is optimized by penalizing energy at non-zero subsurface offset, utilizing the fact that the SODCIGs should

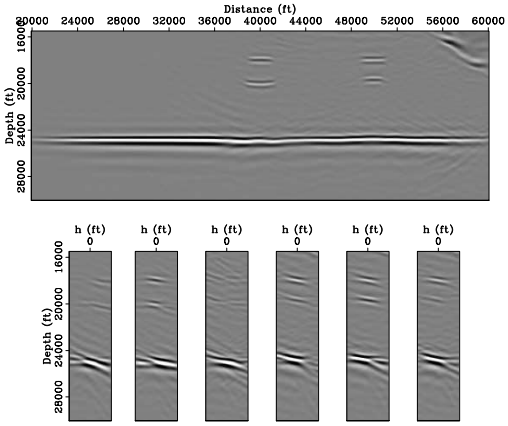

Figure 3: The migrated image and gathers using the new data set. View descriptions are the same as in Figure 2.

be focused at zero subsurface offset if migrated using an accurate velocity model. The DSO objective function reads (Shen, 2004)

$$J_{\mathrm{DSO}}(\mathbf{v}) = \frac{1}{2}\sum_{\widetilde{\mathbf{x}}}\sum_{\mathbf{h}} |\mathbf{h}|^2 \widehat{m}^2(\widetilde{\mathbf{x}},\mathbf{h}), \tag{8}$$

where $\widehat{m}(\widetilde{\mathbf{x}},\mathbf{h})$ is the subsurface-offset-domain image migrated using velocity $\mathbf{v}$ (equation 4) and the Born modeled data described in the previous section. In contrast, minimizing the negative image-stack power (ISP) utilizes the fact that the stacked image should achieve maximum energy (or focus) when migrated with an accurate velocity (Toldi, 1985; Soubaras and Gratacos, 2007). Since the zero-subsurface-offset image is the stacked image, the ISP objective function reads

$$J_{\mathrm{ISP}}(\mathbf{v}) = -\frac{1}{2}\sum_{\widetilde{\mathbf{x}}} \widehat{m}^2(\widetilde{\mathbf{x}},0). \tag{9}$$

The above two objective functions can also be combined into one single objective function as follows (Shen and Symes, 2008):

$$J(\mathbf{v}) = J_{\mathrm{DSO}} + \beta^2 J_{\mathrm{ISP}}, \tag{10}$$

where β is a constant to trade off these two objective functions. The gradients can be calculated using the adjoint-state method without explicitly building the sensitivity matrix, see, e.g. Sava and Vlad (2008); Tang et al. (2008), for implementation details. The gradient is then used to update the velocity model with a suitable step length chosen by a line-search step. We iterate this process until an acceptable velocity model is obtained.

Figure 4 compares the normalized DSO and ISP gradients obtained using the original data set with those obtained using the new data set. These gradients are computed using the starting velocity model (Figure 1(b)). Note that both DSO and ISP gradients correctly identify those two anomalies and they also give correct directions for velocity updates. Also note that, the gradients obtained using the new data set (Figures 4(b) and 4(d)) are very similar to those obtained using the original data set (Figures 4(a) and 4(c)), except that they are obtained

with only 41 plane-wave-source gathers recorded at depth $\widetilde{z}_r =$ 15500 ft instead of 268 point-source gathers recorded at the surface ($z_r = 0$ ft). These examples demonstrate that the new data set can be used for wavefield tomography with much lower computational cost.

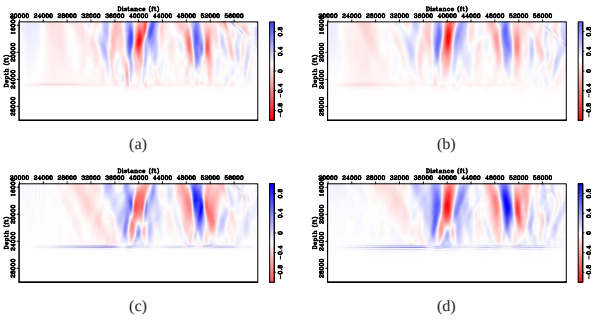

Figure 4: Normalized gradients. Top panels are the DSO gradients obtained using (a) the original data set and (b) the new data set. Bottom panels are the ISP gradients obtained using (c) the original data set and (d) the new data set.

TOMOGRAPHIC INVERSION RESULTS

We have performed wavefield tomography using the new data set modeled from the selected target image as discussed in the previous section. We minimize the combined objective function J (equation 10) using a nonlinear conjugate-gradient solver. Figure 5(a) shows the inverted velocity model after 6 nonlinear iterations and Figure 5(b) shows the true velocity model. The nonlinear inversion has successfully recovered the two anomalies below the salt. The migrated image and gathers using the inverted velocity model and the original data set are shown in Figure 6 (compare it with the results obtained using the starting velocity model shown in Figure 2). The SODCIGs obtained using the inverted velocity model (Figure 6) is more focused at the zero subsurface offset and the horizontal reflector is flatter compared to those obtained using the starting velocity model (Figure 2). For comparison, Figure 7 shows the migration results obtained using the true velocity model.

CONCLUSIONS

We have presented a cost-effective method for image-domain wavefield tomography. Instead of using the original data set for velocity estimation, our method uses demigrated Born data, which can be simulated in a target-oriented fashion and hence much smaller in size. Numerical examples demonstrate that the simulated new data set can successfully preserve velocity information that is useful for velocity analysis and can be used for velocity inversion with low computational cost.

ACKNOWLEDGEMENTS

We thank the sponsors of the Stanford Exploration Project for their support.

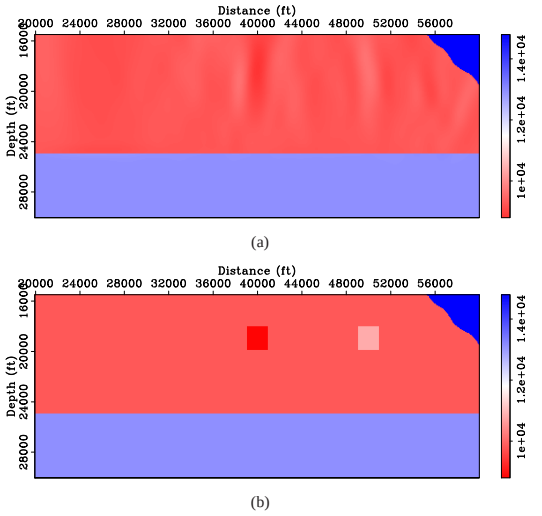

Figure 5: (a) The inverted velocity model and (b) the true velocity model.

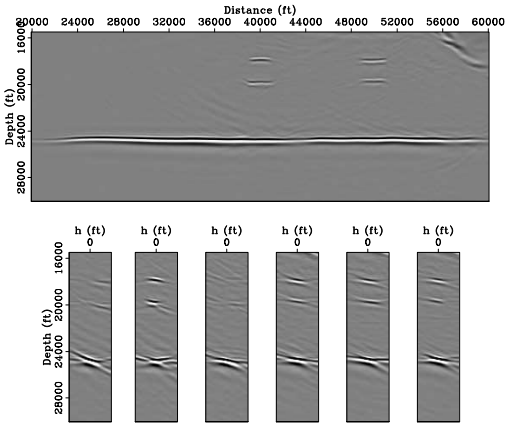

Figure 6: The migrated target image and gathers using the inverted velocity model (Figure 5(a)) and the original data. View descriptions are the same as in Figure 2.

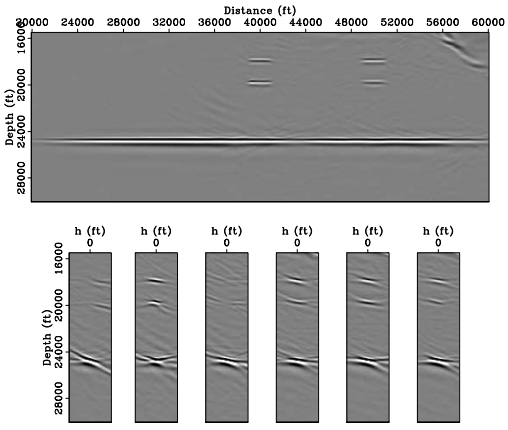

Figure 7: The migrated target image and gathers using the true velocity model and the original data. View descriptions are the same as in Figure 2.

EDITED REFERENCES

Note: This reference list is a copy-edited version of the reference list submitted by the author. Reference lists for the 2010 SEG Technical Program Expanded Abstracts have been copy edited so that references provided with the online metadata for each paper will achieve a high degree of linking to cited sources that appear on the Web.

REFERENCES

Albertin, U., P. Sava, J. Etgen, and M. Maharramov, 2006, Adjoint wave-equation velocity analysis: SEG Technical Program Expanded Abstracts, **25**, no. 1, 3345–3349, doi:10.1190/1.2370226.

Biondi, B., 2002, Stable wide-angle Fourier finite-difference downward extrapolation of 3-D wavefields: Geophysics, **67**, 872–882, doi:10.1190/1.1484530.

Biondi, B., 2006, Prestack exploding-reflectors modeling for migration velocity analysis: SEG Technical Program Expanded Abstracts, **25**, no. 1, 3056–3060, doi:10.1190/1.2370162.

———, 2007, Prestack modeling of image events for migration velocity analysis: SEP-131, 101–118.

Biondi, B., and P. Sava, 1999, Wave-equation migration velocity analysis: SEG Technical Program Expanded Abstracts, **18**, no. 1, 1723–1726, doi:10.1190/1.1820867.

Claerbout, J. F., 1985, Imaging the earth's interior: Blackwell Scientific Publication.

Guerra, C., and B. Biondi, 2008a, Phase-encoding with Gold codes for wave-equation migration: SEP-136, 23–42.

———, 2008b, Prestack exploding reflector modeling: The crosstalk problem: SEP-134, 79–92.

Guerra, C., Y. Tang, and B. Biondi, 2009, Wave-equation tomography using image-space phase encoded data: SEG Technical Program Expanded Abstracts, **28**, 3964–3968.

Hoffmann, J., 2001, Illumination, resolution, and image quality of PP- and PS-waves for survey planning: The Leading Edge, **20**, no. 9, 1008–1014, doi:10.1190/1.1487305.

Lecomte, I., 2008, Resolution and illumination analyses in PSDM: A ray-based approach: The Leading Edge, **27**, no. 5, 650–663, doi:10.1190/1.2919584.

Liu, F., D. W. Hanson, N. D. Whitmore, R. S. Day, and R. H. Stolt, 2006, Toward a unified analysis for source planewave migration: Geophysics, **71**, no. 4, S129–S139, doi:10.1190/1.2213933.

Mora, P., 1989, Inversion = migration + tomography: Geophysics, **54**, 1575–1586, doi:10.1190/1.1442625.

Pratt, R. G., 1999, Seismic waveform inversion in the frequency domain, Part 1: Theory and verification in a physical scale model: Geophysics, **64**, 888–901, doi:10.1190/1.1444597.

Ristow, D., and T. R¨uhl, 1994, Fourier finite-difference migration: Geophysics, **59**, 1882–1893, doi:10.1190/1.1443575.

Romero, L. A., D. C. Ghiglia, C. C. Ober, and S. A. Morton, 2000, Phase encoding of shot records in prestack migration: Geophysics, **65**, 426–436, doi:10.1190/1.1444737.

Sava, P., 2004, Migration and Velocity Analysis by Wavefield Extrapolation: PhD thesis, Stanford University.

Sava, P., and I. Vlad, 2008, Numeric implementation of wave-equation migration velocity analysis operators: Geophysics, **73**, no. 5, VE145–VE159, doi:10.1190/1.2953337.

Shen, P., 2004, Wave-equation Migration Velocity Analysis by Differential Semblance Optimization: PhD thesis, Rice University.

Shen, P., and W. W. Symes, 2008, Automatic velocity analysis via shot profile migration: Geophysics, **73**, no. 5, VE49–VE59, doi:10.1190/1.2972021.

Shen, P., W. W. Symes, S. Morton, A. Hess, and H. Calandra, 2005, Differential semblance velocity analysis via shot profile migration: SEG Technical Program Expanded Abstracts, **24**, no. 1, 2249–2252, doi:10.1190/1.2148164.

Soubaras, R., and B. Gratacos, 2007, Velocity model building by semblance maximization of modulated-shot gathers: Geophysics, **72**, no. 5, U67–U73, doi:10.1190/1.2743612.

Stoffa, P. L., J. T. Fokkema, R. M. de Luna Freire, and W. P. Kessinger, 1990, Split-step fourier migration: Geophysics, **55**, 410–421, doi:10.1190/1.1442850.

Stolt, R. H., and A. Benson, 1986, Seismic Migration: Theory and Practice: Geophysical Press.

Tang, Y., 2008, Modeling, migration and inversion in the generalized source and receiver domain: SEP-136, 97–112.

Tang, Y., 2009, Target-oriented wave-equation least-squares migration/inversion with phase-encoded Hessian: Geophysics, **74**, no. 6, WCA95–WCA107, doi:10.1190/1.3204768.

Tang, Y., C. Guerra, and B. Biondi, 2008, Image-space waveequation tomography in the generalized source domain: SEP-136, 1–22.

Tarantola, A., 1984, Inversion of seismic reflection data in the acoustic approximation: Geophysics, **49**, 1259–1266, doi:10.1190/1.1441754.

Toldi, J., 1985, Velocity analysis without picking: PhD thesis, Stanford University.

Valenciano, A., 2008, Imaging by Wave-equation Inversion: PhD thesis, Stanford University.

Whitmore, N. D., 1995, An Imaging Hierarchy for Common Angle Plane Wave Seismogram: PhD thesis, University of Tulsa.

Woodward, M. J., 1992, Wave-equation tomography: Geophysics, **57**, 15–26, doi:10.1190/1.1443179.

Zhang, Y., J. Sun, C. Notfors, S. H. Grey, L. Chemis, and J. Young, 2005, Delayed-shot 3D depth migration: Geophysics, **70**, no. 5, E21–E28, doi:10.1190/1.2057980.